Current Optics and Photonics
Vol. 3, No. 5, October 2019, pp. 466-472

ISSN: 2508-7266(Print) / ISSN: 2508-7274(Online)
DOI: https://doi.org/10.3807/COPP.2019.3.5.466

Performance of Continuous-wave Coherent Doppler Lidar for Wind Measurement

Shan Jiang[1,2], Dongsong Sun[1]*, Yuli Han[1], Fei Han[1], Anran Zhou[1], and Jun Zheng[1]

[1]*School of Earth and Space Science, University of Science and Technology of China, Hefei 230031, China*
[2]*School of Physics and Material Engineering, Hefei Normal University, Hefei 230601, China*

(Received April 12, 2019 : revised June 11, 2019 : accepted June 19, 2019)

A system for continuous-wave coherent Doppler lidar (CW lidar), made up of all-fiber structures and a coaxial transmission telescope, was set up for wind measurement in Hefei (31.84 N, 117.27 E), Anhui province of China. The lidar uses a fiber laser as a light source at a wavelength of 1.55 μm, and focuses the laser beam on a location 80 m away from the telescope. Using the CW lidar, radial wind measurement was carried out. Subsequently, the spectra of the atmospheric backscattered signal were analyzed. We tested the noise and obtained the lower limit of wind velocity as 0.721 m/s, through the Rayleigh criterion. According to the number of Doppler peaks in the radial wind spectrum, a classification retrieval algorithm (CRA) combining a Gaussian fitting algorithm and a spectral centroid algorithm is designed to estimate wind velocity. Compared to calibrated pulsed coherent wind lidar, the correlation coefficient for the wind velocity is 0.979, with a standard deviation of 0.103 m/s. The results show that CW lidar offers satisfactory performance and the potential for application in wind measurement.

Keywords : Doppler lidar, wind measurement, continuous wave laser, coherent detection, Rayleigh criterion
OCIS codes : (280.3640) Lidar; (280.4788) Optical sensing and sensors; (280.3340) Laser Doppler velocimetry

I. INTRODUCTION

According to the type of laser beam, there are two core coherent lidar technologies, CW lidar and pulsed lidar, both of which are active and accurate in remote measurements of wind in the field [1, 2]. CW lidar uses high-intensity focused beams to target the measurement range, which shows better performance than monostatic collimated pulsed lidar, for the first few hundred meters [3]. CW lidar is widely used in the fields of atmospheric dynamics research, aviation safety, and wind power generation [4, 5]. For example, companies such as ZephIR, Windar Photonics, and Wind cube have developed CW lidar in products for application and extension. In particular, a ZephIR CW lidar with speed range 1~80 m/s was compared to a calibrated ground-based pulsed wind lidar at Natural Power's lidar test site. At the same focusing distance of 82 m, the correlation coefficient was 0.997 for values of the wind velocity [6]. In the same year, a comparison experiment was also carried out for ZephIR 300 lidar and a cup anemometer; the correlation coefficient of the wind velocity was 0.877 under the same temporal resolution of 0.5 s [7]. In addition to the aforementioned experiments, Q. Hu *et al.* developed a CW lidar and compared it to a sonic sensor over a period of 50 minutes at the DTU lidar test site on a clear, sunny afternoon; the experimental results showed the correlation coefficient was 0.862 for wind speeds above 2 m/s under the same temporal resolution 0.5 s [8]. However, CW lidar is sensitive to irregular atmospheric motion. References [8, 9] report that the atmospheric backscattered spectrum generated by CW lidar contains several velocity components under nonlaminar wind flow, but they did not put forward a method for retrieving the radial wind velocity.

With the purpose of improving performance, CW lidar is still being explored. Therefore, a CW lidar with a focal distance of 80 m has been set up for radial wind measurement by our group at USTC (University of Science and Technology of China) in Hefei (31.84 N, 117.27 E),

*Corresponding author: sds@ustc.edu.cn, ORCID 0000-0002-3870-2206
Color versions of one or more of the figures in this paper are available online.

in the Anhui province of China. This study presents the performance of the USTC CW lidar. The structure of this paper is as follows: In section II, the noise floor of the system is tested and the lower limit of wind-velocity measurement is calculated by the Rayleigh criterion through radial measurements; in section III, a classification retrieval algorithm (CRA) is designed to process the irregular Doppler signals from the CW lidar. In section IV, comparison experiments yielding satisfactory results are carried out, with a calibrated pulsed lidar at the same location as a reference; and in section V, we summarize our work.

II. SYSTEM DESCRIPTION AND MEASUREMENT

2.1. System Description

As shown in Fig. 1, the USTC CW lidar system employs an all-fiber CW laser, and consists of a variable optical attenuator in the reference path, which serves as a local oscillator. The light path partly comprises an amplifier and an optical circulator; the other part of the light path is in free space, with the telescope focusing the propagating laser light into the atmosphere and receiving the backscattered light from aerosols. Each port of the circulator is fiber-connected. The working wavelength is 1549 nm, and the focal distance is 80 m. The key parameters of the USTC CW lidar are summarized in Table 1.

The wind velocity measured by CW lidar is integrated along the laser beam according to a range weight function $W(F,R)$ to yield the detected radial velocity $v_{los}(F)$, which is determined by [10]

$$v_{los}(F)=\int_0^{+\infty} v_{los}(R)\,W(F,R)\,dR, \tag{1}$$

where $v_{los}(R)$ is the radial wind speed at a range R along the laser beam, and F is the distance along the beam where the measurement is intended.

Given that the effects of refractive turbulence on laser propagation are ignored, the CW range weight can be approximated by the Lorentz distribution function:

TABLE 1. Key parameters of the USTC CW lidar

Item	Parameters	Value
Laser	Wavelength	1549 nm
	Linewidth	7 kHz @ 1549 nm
	Output power	1 W
Telescope	Effective aperture	70 mm
	Waist radius of Gaussian beam	1.7 cm
	Focal distance	80 m
Balanced detector	3-dB bandwidth	250 MHz
	Responsitivity	0.95 A/W
A/D converter	Sample rate	250 MHz
	Sample precision	14-bit

$$W(F,R)=\frac{K}{R^2+\left(1-\frac{R}{F}\right)^2 R_{Rayleigh}^2}, \tag{2}$$

where $R_{Rayleigh}$ is the Rayleigh length and K is a normalization constant. Note that the value of R in Eq. (2) is a positive number. The Rayleigh length is given by [11]

$$R_{Rayleigh}=\frac{\pi a^2}{\lambda}, \tag{3}$$

where λ is the laser's wavelength and a is the e^{-2}-intensity radius of the Gaussian laser beam. The probe length of CW lidar depends on twice the Rayleigh length from which most of the backscattered signals originate [12].

CW systems have an inherent maximum range (on the order of a few hundred meters), beyond which it is impossible to focus the beam, because of diffraction [13]. According to the spatial weight distribution of the CW laser, the normalized weight function for the USTC CW lidar depending on the focal distance is illustrated in Fig. 2, and the probe length is also indicated with lines above.

It is straightforward to see that as the focal distance increases, the detected velocity contains more contributions from a greater length along the beam, and the lidar becomes more sensitive to irregular atmospheric motion in the radial direction. According to the key parameters listed

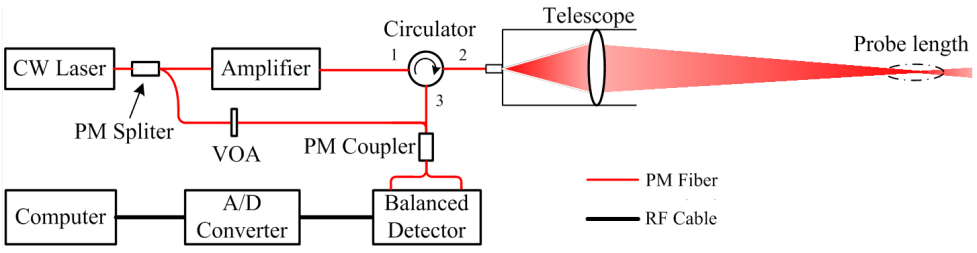

FIG. 1. Schematic diagram of the USTC CW lidar: VOA, variable optical attenuator; PM, Polarization maintain; RF, radio frequency; A/D, analog to digital.

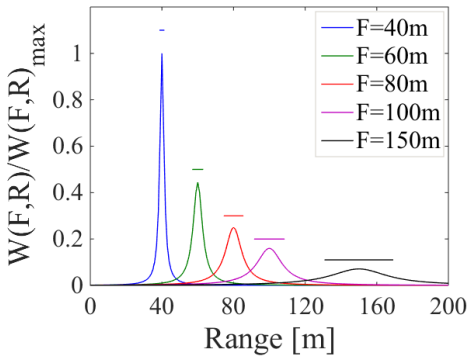

FIG. 2. Normalized range weight functions for the USTC CW lidar, depending on the focal distance, with the probe length indicated with a line above each trace.

in Table 1, the Rayleigh length of the USTC CW lidar is 5.46 m and the probe length is 10.93 m. It is reported that radial wind spectrum contains several Doppler peaks, from a ZephIR CW lidar with a probe length greater than 10 m [9]. Therefore, the USTC CW lidar's performance in radial wind measurement should be tested in detail.

2.2. Radial Wind Measurement

Radial wind measurement using the USTC CW lidar was performed in Hefei (31.84 N, 117.27 E), in Anhui province of China in 2019. Typical raw data are shown in Fig. 3.

Under laminar wind flow, the spectrum contains one typical Doppler peak, as shown in Fig. 3(a), and it is easy to retrieve the radial velocity. Meanwhile, under nonlaminar wind flow the wind spectra were irregular and more turbulent; in Figs. 3(b) and 3(c), the spectra contain several speed components. Essentially, retrieval of the radial wind velocity is a frequency-estimation problem for weak signals. Usually only one estimated value is used to represent the wind velocity in the radial direction. The radial wind spectrum from CW lidar often contains several speed components under nonlaminar flow, which rarely appears in pulsed lidar. Hence an appropriate algorithm to estimate the center frequency of each Doppler signal must be developed for CW lidar systems.

A considerable amount of excess noise, which induced large fluctuations, was observed in the low-frequency range of the radial wind spectrum, as shown in Fig. 4. Occasionally the low-frequency noise energy was equal to or greater than that of the atmospheric backscattered signal. When the wind velocity was below a certain value, the noise even overlapped or covered the Doppler signal, as shown in Figs. 4(b) and 4(c). This type of excess noise has been denoted as phase-induced intensity noise (PIIN) in reference [14]. The performance of coherent Doppler lidar is optimal when the system reaches the shot-noise limit [15]. Through our experiment, PIIN may be a few orders of magnitude higher than shot-noise level. Hence other noise, including shot noise, can be omitted, and PIIN needs to be analyzed carefully. Based on the above analysis, the blind zone of the lidar system in wind velocity measurement can be deduced.

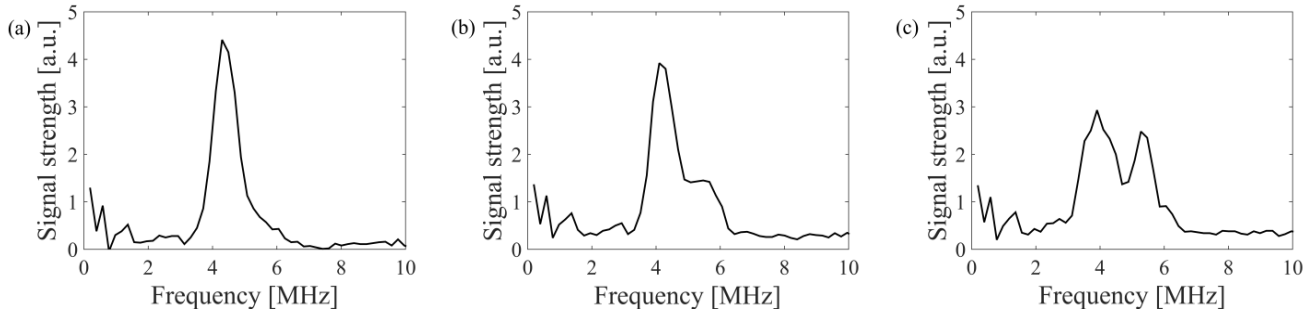

FIG. 3. Radial wind spectra measured by the USTC CW lidar: (a) The spectrum contains one Doppler peak for laminar wind, while several Doppler peaks appear for nonlaminar wind in (b) and (c).

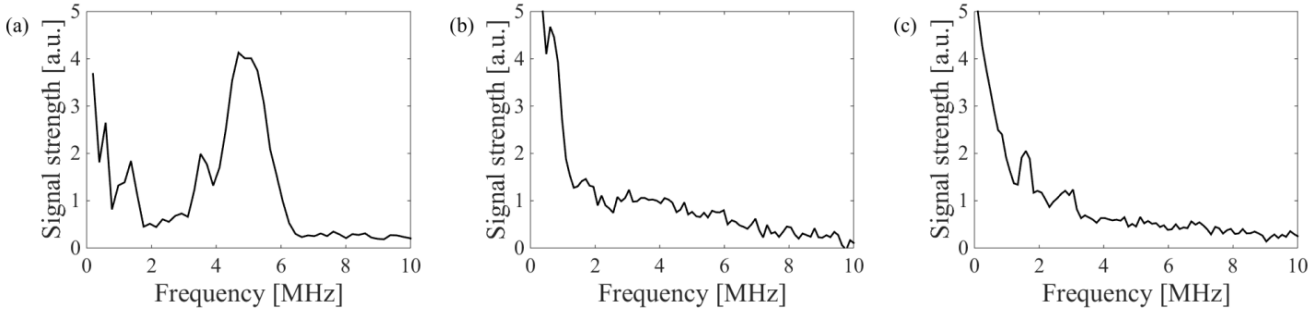

FIG. 4. Radial wind spectra with excess low-frequency noise. The low-frequency noise energy is almost equal to the energy of the atmospheric backscattered signals in (a), while they overlap in (b), and the signal is covered in (c).

2.3. Noise Analysis

As shown in Fig. 1, a fiber-optic circulator is employed in the USTC CW system. Most of the laser power takes the route from port 1 to port 2, while a tiny fraction of light from port 1 leaks into port 3. The leaked light is coherent with the local oscillator, which introduces excess intensity noise that is much greater than the shot-noise level. Since the phase noise tends to be stronger, as it is closer to the center wavelength of the laser, PIIN tends to be stronger, as it is closer to zero frequency in the mixing signal spectrum of the coherent system. We occluded the telescope and averaged noise spectra after noncoherent accumulation. The averaged noise spectra are shown in Fig. 5.

Both the PIIN and the backscattered signal are emitted through the 3-port fiber of the circulator. Both of them can be considered Fraunhofer circular-aperture diffraction and have the same intensity distribution. Due to the resolution limit, the diffraction images of two pointlike sources (Airy disks) cannot be resolved when they are too close, so it is difficult to distinguish wind-velocity signals from noise if the Doppler frequency is lower than a certain value. According to the Rayleigh criterion, when the maximum of intensity of one source overlaps the first intensity minimum of a second bright source, as shown in Fig. 6, we can obtain the smallest resolution angle $\Delta\theta$ [16]:

$$\Delta\theta = 1.22\frac{\lambda}{D}, \tag{4}$$

where D is the mode-field diameter of the fiber. The light from the fiber's end can be approximated by the intensity distribution of Fraunhofer circular aperture diffraction, as per Eqs. (5) and (6):

$$I = I_0\left[\frac{2J_1(x)}{x}\right]^2, \tag{5}$$

$$x = \pi D\frac{\sin\theta}{\lambda}, \tag{6}$$

where I_0 is the output light intensity from the fiber, $J_1(x)$ is the first-order Bessel function, and θ is the diffraction angle. In the case of resolution limit $\theta = \Delta\theta$, the ratio R_{sp} between the saddle point and peak of the envelope can be determined to be 0.734.

After scaling to the Bessel function, the intensity distribution of the two signals (ideal atmospheric backscattered signal and ideal PIIN) are compared in Fig. 7. According to the ratio R_{sp}, the upper-limit frequency f_b of the blind zone can be calculated as 0.930 MHz, which corresponds to 0.721 m/s. At airports or wind power plants, wind speeds less than 0.721 m/s are rare, so the USTC CW lidar has high utility with such a blind zone in wind measurement.

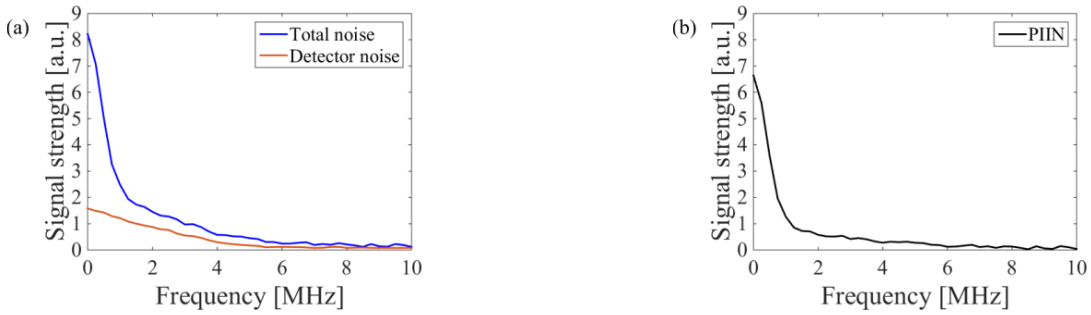

FIG. 5. Total noise is measured with the telescope occluded in (a), as well as the detector noise (noise from photodetector and other electric components) when the local oscillator does not emit light. PIIN is obtained by subtracting the detector noise from the total noise, in (b).

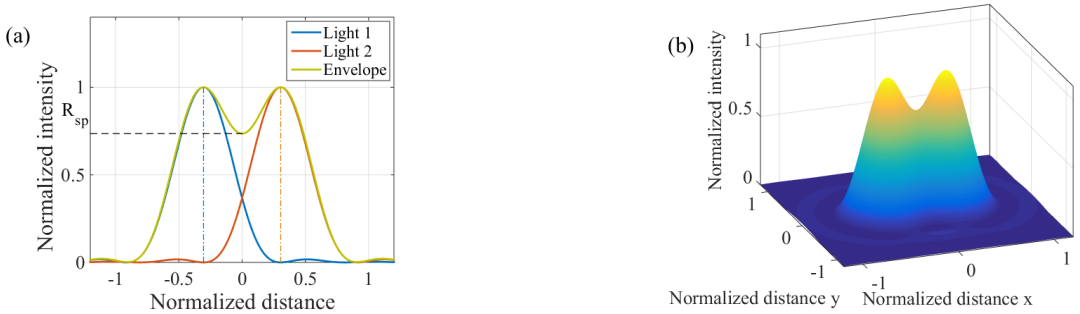

FIG. 6. Resolution limit based on the Rayleigh criterion: (a) profile map, (b) three-dimensional map.

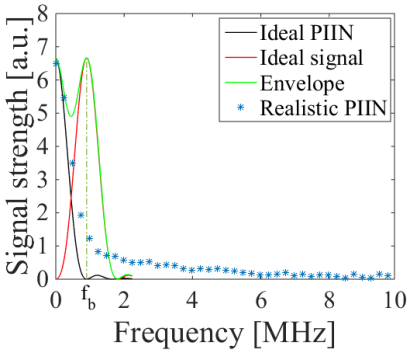

FIG. 7. After scaling, the ideal PIIN and ideal atmospheric backscattered signal are compared. Realistic PIIN is also indicated by snowflake symbols.

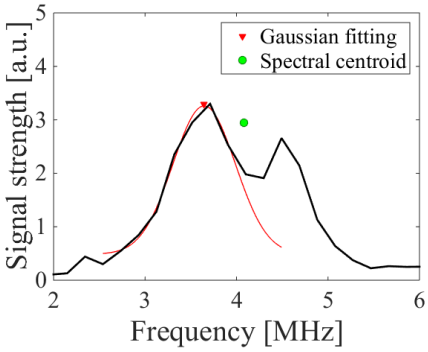

FIG. 8. The center frequency, calculated by different algorithms. Gaussian fitting still extracts the frequency of the Doppler peak with highest power (indicated by a red triangle), while the spectral centroid result represents the center frequency better (indicated by a green dot).

III. WIND-VELOCITYRETRIEVAL ALGORITHM

The typical Doppler signal received by CW lidar can be fitted with a Gaussian distribution as a frequency-dependent reflection coefficient [16]. By virtue of the literature [17], wind velocity can be estimated by Gaussian fitting for single-peak Doppler signals:

$$I(f,f_{Doppler})=\beta\lambda^2\frac{f_{bin}}{2\sqrt{2\pi\sigma^2}}exp\left(-2\alpha F+\frac{\lambda^2(f-f_{Doppler})}{8\sigma^2}\right), \quad (7)$$

where β and α are respectively the backscattered and extension coefficients of the atmospheric air for a laser wavelength of 1550 nm. f_{bin} is the frequency bandwidth of each frequency bin in the FFT power spectrum of the detector signal, $f_{Doppler}$ is the center Doppler frequency of the measured spectrum, and σ is the standard derivation of the wind velocity along the measuring volume. However, if a Doppler-signal spectrum contains several peaks, the algorithm generates large errors, as shown in Fig. 8, because Gaussian fitting still extracts the frequency of the Doppler peak with highest power, which obviously cannot represent the center frequency of the entire spectrum under nonlaminar wind flow. The spectral centroid is an important feature of signal-frequency domain analysis [18, 19]. It is defined as the weighted average frequency within a given bandwidth, where the weight is the energy of each frequency component. The center frequency of the discrete spectrum's centroid can be expressed as [20]

$$f_{SC}=\frac{\sum_{f_i=f_1}^{f_2}f_i\cdot S(f_i)}{\sum_{f_i=f_1}^{f_2}S(f_i)}, \quad (8)$$

where f_{SC} is the frequency of the spectral centroid, f_1 and f_2 are the upper and lower limits of the given bandwidth, and $S(f_i)$ is the signal energy at the frequency f_i. Taking the signal in Fig. 8 as an example, we used the spectral centroid algorithm to estimate radial wind velocity as follows:

1. Search the peaks and identify x_1, x_2 as the frequencies corresponding to the peaks;
2. Search the valley and identify x_0 as the frequency corresponding to the valley;
3. Select points between x_1 and x_0, and select the same number of points to the left of x_1;
4. Select points between x_0 and x_2, and select the same number of points to the right of x_2;
5. The spectral centroid algorithm then yields the radial wind velocity as

$$v_{los}=\frac{\lambda}{2}\cdot\left[\frac{\sum_{f_i=x_1-\frac{N_1\cdot F}{N}}^{x_2+\frac{N_2\cdot F}{N}}f_i\cdot S(f_i)}{\sum_{f_i=x_1-\frac{N_1\cdot F}{N}}^{x_2+\frac{N_2\cdot F}{N}}S(f_i)}\right], \quad (9)$$

where F is the sampling rate, N is the total number of points of the FFT power spectra, N_1 is the number of points between x_1 and x_0, and N_2 is the number of points between x_2 and x_0. The processing result of the spectral centroid estimation algorithm is also showed in Fig. 8. It can be seen that the spectral centroid better represents the center frequency of irregular Doppler shifts for nonlaminar wind.

To enhance the wind-measurement reliability and accuracy of CW lidar under laminar and nonlaminar flow, a classification retrieval algorithm (CRA) is designed that estimates the wind velocity according to the number of Doppler peaks. First, the raw data is preprocessed to remove the noise floor. Second, the number of Doppler-shift peaks in the backscattered signal spectrum is deduced, and the threshold is set to eliminate noise interference. Finally, the algorithm is classified according to the number of Doppler peaks, *i.e.* Gaussian fitting for a single-peak spectrum, and the spectral centroid algorithm for a multipeak spectrum.

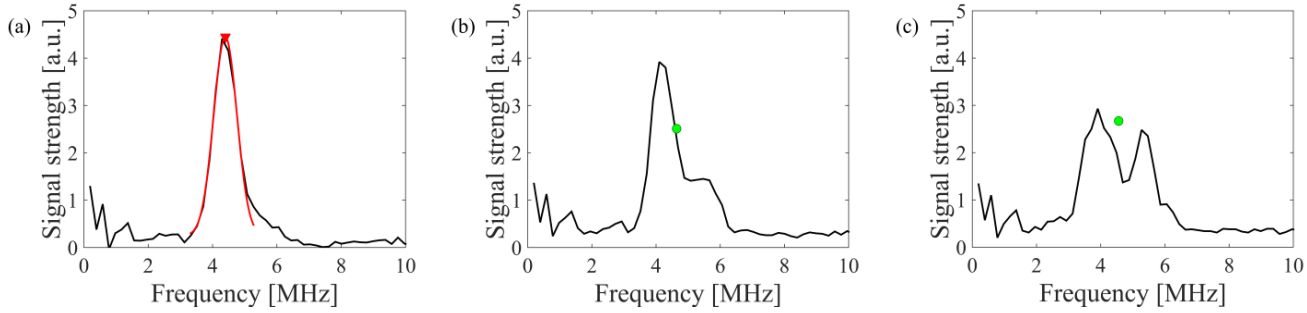

FIG. 9. The center frequency calculated by CRA.

The proposed algorithm is used to process the raw data in Fig. 3, and the results are shown in Fig. 9. The red triangle denotes the frequency corresponding to the radial wind velocity calculated by the Gaussian fitting algorithm in Fig. 9(a), while the green circle represents the frequency calculated by the spectral centroid algorithm in Figs. 9(b) and 9(c). It can be seen that CRA can extract the center frequency of the Doppler signal, and would be suitable for velocity retrieval whether the wind flow is laminar or not.

IV. EXPERIMENT AND DISCUSSION

Aiming to validate the performance of the USTC CW lidar, experiments comparing it and a pulsed lidar were carried out at the same location on the morning of January 18th, 2019. The pulsed lidar we used was compared to ultrasonic anemometers on the meteorological observational tower in Shenzhen (22.65 N, 113.90 E), China. The correlation coefficient for wind velocity measured by the pulsed lidar and ultrasonic anemometers is 0.980, with a standard deviation of 0.235 m/s. The key parameters of the pulsed lidar system are showed in Table 2.

The telescopes of the USTC CW lidar and the pulsed lidar were mounted in parallel, as shown in Fig. 10.

In Fig. 11, data series from the USTC CW lidar processed by CRA for a duration of 60 minutes are shown, including the pulsed-lidar data, which are limited to the 60~90 m distance gate, as reference. Data of center frequency less than 0.930 MHz, corresponding to velocity less than 0.721 m/s, have been removed.

We can observe very high wind-data correlation between the two lidars at a 1-Hz update rate. The correlation coefficient for wind velocity measured by the two lidars is 0.979, with a standard deviation of 0.103 m/s. From Fig. 11, we can conclude that the maximum difference appears at 15:52:04, and is 0.481 m/s. The results further confirm that the USTC CW lidar has perfect performance in measuring the temporal evolution of the radial wind velocity.

TABLE 2. Key parameters of the pulsed lidar

Item	Parameters	Value
Laser	Wavelength	1547 nm
	Linewidth	4 kHz @ 1547 nm
	Pulse energy	150 μJ
	Pulse width	200 ns
	Pulse repetition frequency	10 kHz
Telescope	Effective aperture	70 mm
Balanced detector	3-dB bandwidth	250 MHz
	Responsitivity	0.95 A/W
A/D converter	Sample rate	250 MHz
	Sample precision	14-bit

FIG. 10. The installation mode of the lidar telescopes.

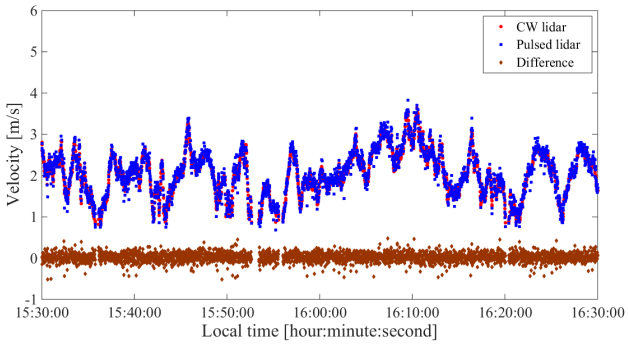

FIG. 11. Wind-velocity-measurement comparison between the USTC CW lidar and the pulsed lidar, over a period of 60 minutes. The difference is indicated by the brown spots.

V. CONCLUSION

In summary, the USTC CW lidar with 80-m focal distance is described. Through radial wind measurement, irregular Doppler signals and excess low-frequency noise were observed and analyzed. We tested the noise and introduced the Rayleigh criterion into signal distinction to resolve the lidar's lower limit of velocity measurement (0.721 m/s). The applicabilities of the Gaussian fitting algorithm and spectral centroid algorithm are compared in radial-wind-velocity retrieval under nonlaminar wind flow. The CRA is designed and applied to the USTC CW lidar. Comparison experiments were performed with a calibrated pulsed lidar as reference. The correlation coefficient for radial wind velocity measured by the two systems was 0.979, and the standard deviation 0.103 m/s, which show high consistency. Thus the USTC CW lidar displays stable operation and yields reliable results that will be suitable for wind measurement.

ACKNOWLEDGMENT

It is my pleasure to thank Dr. J. S. Feng for his helpful comments on the paper. This work is supported by the National Natural Science Foundation of China (41774193) and key projects of natural science research in Colleges and Universities of Anhui province (KJ2019A0724).

REFERENCES

1. C. Hill, "Coherent focused lidars for Doppler sensing of aerosols and wind," Remote Sens. **10**, 466 (2018).
2. X. D. Jia, D. S. Sun, Z. F. Shu, F. F. Zhang, and H. Y. Xia, "Optimal design of the telescope in coherent lidar and detection performance analysis," ATCA Opt. Sin. **35**, 0301001 (2015).
3. E. Brinkmeyer and T. Waterholter, "Continuous wave synthetic low-coherence wind sensing Lidar: motionless measurement system with subsequent numerical range scanning," Opt. Express **21**, 1872-1897 (2013).
4. P. J. Rodrigo, T. F. Q. Iversen, Q. Hu, and C. Pederson, "Diode laser lidar wind velocity sensor using a liquid-crystal retarder for non-mechanical beam-steering," Opt. Express **22**, 26674-26679 (2014).
5. T. Beuth, M. Fox, and W. Stork, "Parameterization of a geometrical reaction time model for two beam nacelle lidars," Proc. SPIE **9612**, 96120J (2015).
6. M. Pitter, E. B. des Roziers, and J. Medley, "Performance stability of ZephIR in high motion environments: floating and turbine mounted," in Proc. *EWEA Annual Event* (Barcelona, Spain, 2014), pp. 1-13.
7. W. Barker, M. Harris, M. Pitter, E. B. des Roziers, J. Medley, and C. Slinger, "Lidar turbulence measurements for wind turbine selection studies: design turbulence," in Proc. *EWEA Annual Event* (Barcelona, Spain, 2014), PO.ID: 169.
8. Q. Hu, P. J. Rodrigo, and C. Pedersen, "Remote wind sensing with a CW diode laser lidar beyond the coherence regime," Opt. Lett. **39**, 4875-4878 (2014).
9. M. Harris, M. Hand, and A. Wright, "Lidar for turbine control," in *National Renewable Energy Laboratory, Technical Report* (Golden, USA, Jan. 2006), TP500-39154.
10. R. G. Frehlich and M. J. Kavaya, "Coherent laser radar performance for general atmospheric refractive turbulence," Appl. Opt. **30**, 5325-5352 (1991).
11. E. Simley, L. Y. Pao, R. Frehlich, B. Jonkman, and N. Kelley, "Analysis of light detection and ranging wind speed measurements for wind turbine control," Wind Energy **17**, 413-433 (2014).
12. P. Lindelöw, "Fiber based coherent lidars for remote wind sensing," Ph. D. Thesis (Technical University of Denmark, Denmark, 2007).
13. R. Frehlich, M. H. Stephen, and S. W. Henderson, "Coherent Doppler lidar measurements of winds in the weak signal regime," Appl. Opt. **36**, 3491-3499 (1997).
14. P. J. Rodrigo and C. Pedersen, "Reduction of phase-induced intensity noise in a fiber-based coherent Doppler lidar using polarization control," Opt. Express **18**, 5320-5327 (2010).
15. S. W. Henderson, P. Gatt, D. Rees, and R. M. Huffaker, *Laser remote sensing*, T. Fujii, T. Fukuchi, ed. (CRC Press, Taylor & Francis Group, New York, USA, 2005), Chapter 7.
16. F. Tamburini, G. Anzolin, G. Umbriaco, A. Bianchini, and C. Barbieri, "Overcoming the Rayleigh criterion limit with optical vortices," Phys. Rev. Lett. **97**, 163903 (2006).
17. R. S. Hansen and C. Pedersen, "All semiconductor laser Doppler anemometer at 1.55 μm," Opt. Express **16**, 18288-18295 (2008).
18. D. Hosseinzadeh and S. Krishnan, "On the use of complementary spectral features for speaker recognition," EURASIP J. Adv. Signal Process. **2008**, 258184 (2007).
19. J. S. Seo, M. Jin, S. I. Lee, D. Jang, S. J. Lee, and C. D. Yoo, "Audio fingerprinting based on normalized spectral sub-band centroids," in *Proc. IEEE International Conference on Acoustics, Speech, and Signal Processing* (USA, Mar. 2005), pp. 213-216.
20. W. Flores-Fuentes, M. Rivas-Lopez, O. Sergiyenko, F. F. Gonzalez-Navarrob, J. Rivera-Castillob, D. Hernandez-Balbuena, and J. C. Rodríguez-Quiñoneza, "Combined application of power spectrum centroid and support vector machines for measurement improvement in optical scanning systems," Signal Process. **98**, 37-51 (2014).